Title

Residual lattice strain in quartzites as a potential palaeo-piezometer

Journal

Geophysical Journal International, 222(2)

ISSN

0956-540X

Authors

Wenk, Hans-Rudolf
Chandler, Brian Chase
Chen, Kai
et al.

Publication Date

2020-08-01

DOI

10.1093/gji/ggaa226

Peer reviewed

Geophysical Journal International

Geophys. J. Int. (2020) **0,** 1–16
Advance Access publication 2020 May 09
GJI Rock and Mineral Physics, Rheology

doi: 10.1093/gji/ggaa226

Residual lattice strain in quartzites as a potential palaeo-piezometer

Hans-Rudolf Wenk[1], Brian Chase Chandler,[1] Kai Chen,[2] Yao Li,[2,3] Nobumichi Tamura[4] and Rong Yu[1,5]

[1]*Department of Earth and Planetary Science, Univ. California, Berkeley CA* 94720*, USA. E-mail: wenk@berkeley.edu*
[2]*State Key Laboratory for Mechanical Behavior of Materials, Xi'an Jiaotong University, Xi'an* 710049*, PR China*
[3]*School of Materials Science and Engineering, Chang'an University, Xi'an, Shaanxi* 710064*, PR China*
[4]*Advanced Light Source, Lawrence Berkeley Laboratory, Berkeley CA* 94720*, USA*
[5]*Xi'an Polytechnic University, Xi'an* 710048*, PR China*

Accepted 2020 May 5. Received 2020 April 29; in original form 2020 January 13

SUMMARY

If a crystal lattice is subjected to a stress, it becomes distorted and no longer represents the ideal crystal symmetry, and if the stress introduces defects such as dislocations, some of this distortion is preserved after the applied stress is removed. In this study, we investigate lattice distortion in quartz at the micron scale with synchrotron X-ray Laue diffraction. From Laue images the local deviatoric strain tensor is derived and corresponding stresses are calculated based on elastic properties. The method is applied to metasedimentary quartzites from the Bergell Alps that were deformed at conditions of greenschist facies metamorphism. The residual palaeostrain is represented in maps of the deviatoric strain tensor components and with deviatoric strain axis pole figures. Data suggest overall shortening perpendicular to the schistosity plane but with considerable asymmetry relative to foliation and lineation, probably attributed to simple shear. Crystallographic pole figures from Laue diffraction agree with neutron diffraction and EBSD measurements and display quartz **c**-axes girdle distributions with maxima also perpendicular to schistosity. The method shows promise to be used as a palaeo-piezometer to unravel the stress field during tectonic deformation.

Key words: Defects; Elasticity and anelasticity; Geomechanics; Mechanics, theory, and modelling; Microstructures.

1 INTRODUCTION

If a crystalline material is subjected to stress, the crystal structure becomes distorted. For example, in the case of cubic crystals lattice angles are no longer 90° and the unit cell constants are no longer equal. If stresses are low and within the elastic limit, the lattice returns to the original shape upon reversal. However, if stresses are higher, they impose local defects in crystals such as dislocations, disclinations, twins, planar defects, grain boundary structures (e.g. Kröner & Anthony 1975). In this case, upon removal of stress, some of the lattice strain is preserved, being trapped by the defects. Lattice distortion can be imposed by macroscopic deformation, caused by temperature–pressure changes or by phase transitions.

Residual stress has been an important topic in materials science and was studied in great depth in metals, since lattice distortions reduce the mechanical stability of materials (e.g. Noyan & Cohen 1987; Hosford 2005; Withers 2007). How does residual stress affect material performance? Concerns range from stresses in thin films (e.g. Kang *et al.* 2003), welds (e.g. Staron *et al.* 2002), to railway rails (e.g. Kelleher *et al.* 2003) and bridges (e.g. Van Puymbroeck *et al.* 2019).

There is a range of methods to measure residual strain (e.g. Schajer 2013). Most important are diffraction methods which directly observe lattice distortion through peak shifts and peak broadening. Among those methods are neutron diffraction (e.g. Pintschovius & Jung 1983; Clausen *et al.* 1999; Withers & Webster 2001; Hutchings *et al.* 2005), X-ray diffraction peak broadening (e.g. Ungar *et al.* 2001), synchrotron X-ray diffraction (e.g. Stefanescu *et al.* 2004; Ice *et al.* 2011), high resolution electron backscatter diffraction (EBSD) with a scanning electron microscope (e.g. Wilkinson *et al.* 2006; Britton & Wilkinson 2011; Britton *et al.* 2013; Wallis *et al.* 2017) and focused ion beam (FIB) milling (e.g. Kruhl *et al.* 2013; Lunt & Korsunsky 2015).

In this study, we are using microfocus synchrotron Laue diffraction to investigate potential residual strains preserved in deformed metamorphic rocks. We originally became interested in Laue diffraction by investigating metamorphic quartzites from the Alps and observing strong spreading of diffraction peaks, attributed to lattice distortions (Wenk 1966). Much later we used Laue diffraction more quantitatively to explore magnitudes of residual lattice strains in deformed granite, documenting lattice strains of ∼900 microstrains, corresponding to residual stress of ∼50 MPa (Kunz *et al.*

Figure 1. Hand specimen of sample Sci690 with foliation and pronounced lineation. The black line marks strike and dip in the field.

2009). We followed up with quartz associated with the San Andreas fault and observed stresses of ∼120 MPa (Chen *et al.* 2015) and the Vredefort meteorite impact site with stresses up to 250 MPa (Chen *et al.* 2011). These studies focused on stress magnitudes but information from Laue images also provides stress orientations relative to sample coordinates. An exploratory investigation was carried out on deformed quartz from the classical locality in Bastogne, Belgian Ardennes, where boudinage was first described (Lohest *et al.* 1908). Interestingly Laue diffraction results (Chen *et al.* 2016b) indicated that quartz in Bastogne boudins was subjected to compression along the boudinage axis, rather than extension, as in layered metamorphic rocks (e.g. Goscombe *et al.* 2004; Fossen 2016), which is in agreement with strains inferred by Bruehl (1969) for Bastogne boudinage.

This first application of Laue diffraction to map the orientation of the residual strain ellipsoid encouraged a more systematic investigation, advancing and generalizing the technique to evaluate general states of residual lattice strain. Here we apply the method to a series of metamorphic quartzites from the central Alps for which textures and microstructures have been analysed with neutron diffraction and EBSD (Wenk *et al.* 2019).

2 EXPERIMENTS AND DATA ANALYSIS

2.1 Samples

This study relies on seven samples of quartzite from Val Bregaglia in the central Alps. They were originally Triassic sandstones that deformed at greenschist facies metamorphic conditions during the Alpine orogeny 20–60 Ma, producing characteristic microstructures and crystallographic preferred orientation. The quartzite samples display a strong foliation and a lineation (Fig. 1), indicating complex deformation conditions. Preferred orientation was studied in detail by neutron diffraction and scanning electron microscopy with electron backscatter diffraction (EBSD, Wenk *et al.* 2019). In this investigation, we rely on thin sections cut perpendicular to the foliation plane and parallel to the lineation. Optical microscopy shows microstructures with significant recrystallization (Fig. 2). Most quartz displays flattened grains with undulatory extinction due to significant plastic deformation. In many samples quartz also has optically visible deformation lamellae (e.g. Brg1137 in Fig. 2) indicative of high stress (e.g. Christie and Ardell 1974; Hamers & Drury 2011; Derez *et al.* 2015, Chen *et al.* 2016a). Muscovite alignment defines the schistosity plane. In Sci881 the muscovite microstructure also suggests some simple shear deformation. TEM studies on similar samples revealed high dislocation densities, sometimes with concentrations near subgrain boundaries (Fig. 3, Liddell *et al.* 1976). Some details about the samples are listed in Table 1, including localities with Swiss geographic coordinates (in km), scan geometry and quartz preferred orientation based on neutron diffraction.

2.2 Laue diffraction experiments

X-ray microdiffraction (μXRD) measurements in Laue (polychromatic) mode were conducted on beamline 12.3.2 of the Advanced Light Source synchrotron at Lawrence Berkeley National Laboratory. A polychromatic (5–24 keV) X-ray beam is focused to a spot size of 1 μm × 1 μm using a pair of Kirkpatrick-Baez mirrors. The samples consist of uncovered petrographic thin sections ∼30 μm in thickness mounted with epoxy on a glass slide. Each sample was then mounted on a translational scanning stage tilted 45°, and positioned at the focal point of the X-ray beam (Fig. 4). Since the polychromatic X-ray beam size is much smaller than the crystal size, in most cases more or less single crystal Laue diffraction patterns are recorded in reflection geometry at each position with a 2-D Pilatus 1 M detector, placed about 15 cm above the specimen, at 90° with respect to the incident X-ray beam. The X-ray penetrates the 30 μm thin section and causes a dark alteration in the glass beneath it and therefore diffraction pattern averages over the sample thickness. The experimental geometry (detector distance and orientation, incident X-ray beam position) were calibrated using a synthetic silicon crystal or a quartz single crystal assumed to be strain-free.

A question which is often asked: Why using Laue diffraction with polychromatic X-rays rather than monochromatic X-rays which are standard for most crystallographic studies? The answer is Bragg's law $2d_{hkl}\ \sin\theta\ = \lambda$, relating the wavelength λ to the angle 2θ at which diffraction occurs on a lattice plane hkl with a spacing d_{hkl}. But Bragg's law also requires that the lattice plane has to be in a reflection orientation. In general this condition is not satisfied and the crystal needs to be rotated to get diffraction; or a powder is used where some crystallites have the correct orientation. With microdiffraction, where we are investigating the crystal lattice at a micron scale, we can not tilt or rotate significantly without changing the analysed volume and increasing the time greatly (currently ∼1 s per spot). Thus we are returning to polychromatic radiation where the Bragg conditions are relaxed, and without which Friedrich *et al.* (1912) could not have recorded the first diffraction images.

Some microfocus Laue diffraction images of quartz are shown in Fig. 5. Note that the Pilatus detector divides the image into 10 sectors with blind stripes in between. Diffraction from a quartz single crystal used as a standard produces very sharp spots (Fig. 5a). Such patterns can be indexed and define the quartz crystal lattice (some spots are labeled). On Laue images from deformed quartzites there is a wide range of patterns with significant streaking, indicative of bending of the lattice (Figs 5b–d). Some images display splitting of reflections suggesting differently oriented domains (Fig. 5b).

Exposure times are ∼1 s and scans are performed by translating the sample in small increments over a chosen area (Table 1). The scanned area includes several crystals. Scanning over 1 mm^2 in 10 μm steps takes several hours and produces a large set of data that need to be analysed.

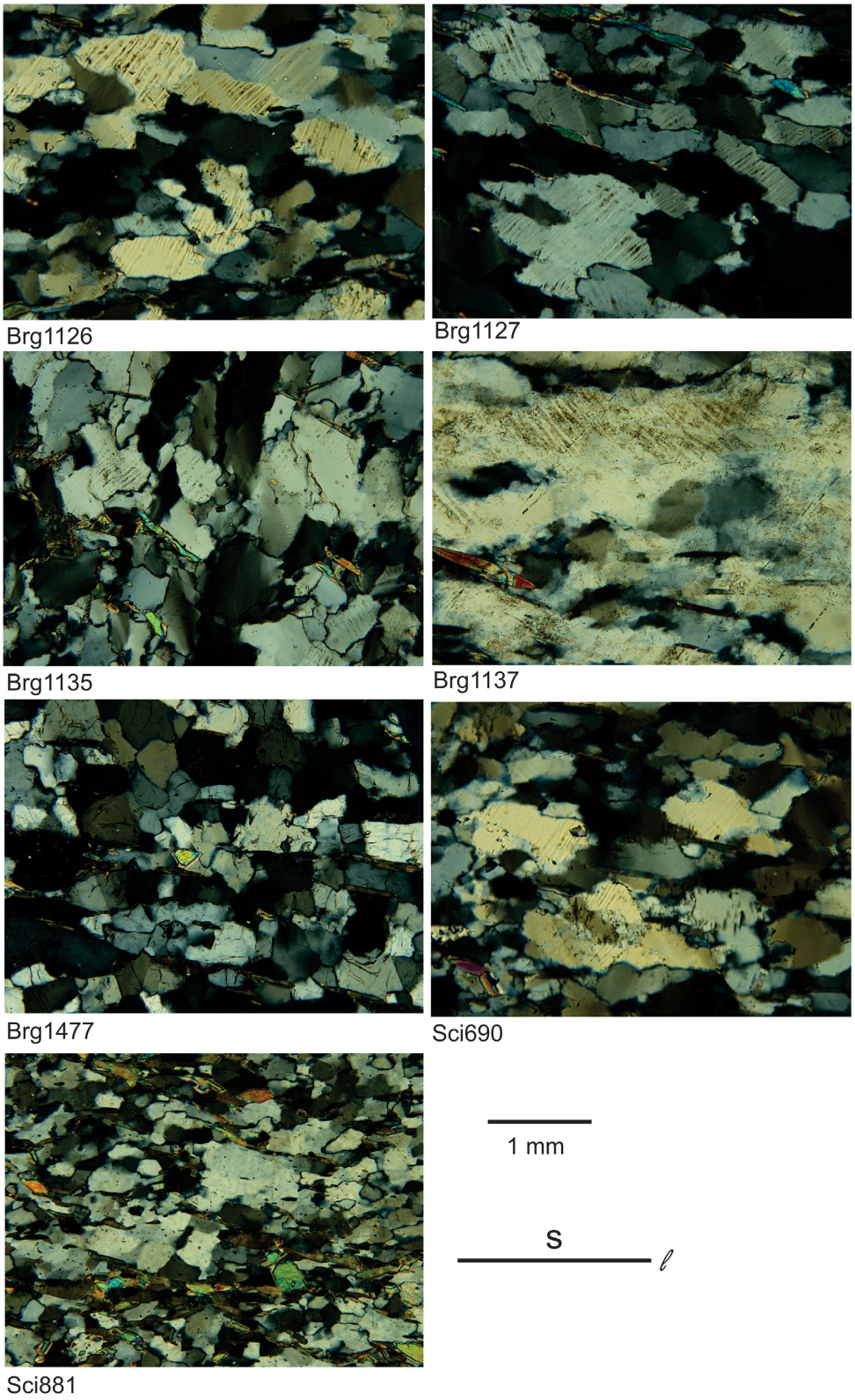

Figure 2. Microstructures of quartzites observed with optical microscopy, crossed polarized light. Note planar deformation lamellae in several samples. Schistosity s and lineation l.

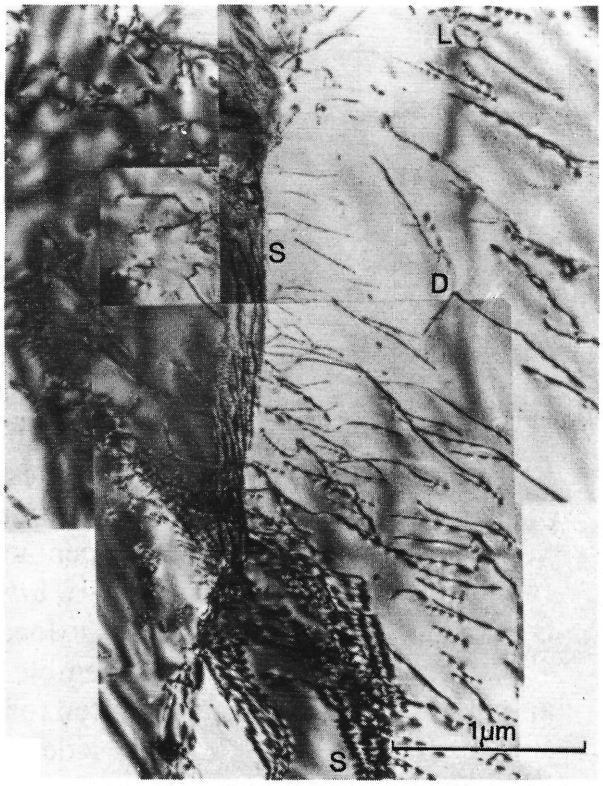

Figure 3. TEM image of dislocation structures in quartzite Sci881 (from Liddell *et al.* 1976). D is a point with dislocation interaction, S a subgrain boundary and L a dislocation loop.

2.3 From lattice distortion to strain tensor geometry

Lattice distortion in deformed samples can arise from either elastic or plastic deformation. In general elastic deformation causes deviations in lattice parameters and unit cell angles (Fig. 6a) that are restored once the force causing it is removed. But if deformation causes irreversible microstructural defects such as disclinations and dislocations like those illustrated in Fig. 3, deformation lamellae (Fig. 2), microscopic twins, stacking faults or point defects (e.g. associated with OH substitution of oxygen), it can impart elastic strains which are preserved (residual strains) and correspondingly also residual stresses. This residual strain manifests as a shifting of the diffraction spots from their unstrained, or reference, positions. The angular deviation imparted by this shift is then used to determine the strain within the crystal lattice (Tamura 2014).

In order to investigate the residual strain, we must determine the lattice distortion and compare it with an unstrained, or reference, lattice. Since the energies associated with each diffraction spot are not known, the Laue method cannot detect dilatational changes of the unit cell volume ($\varepsilon_{ij}^{dil.}$) but instead probes the lattice shape distortion represented by the deviatoric strain tensor ε_{ij}^{dev}. The total strain tensor is the sum of these two parts:

$$\varepsilon_{ij} = \varepsilon_{ij}^{dil.} + \varepsilon_{ij}^{dev}, \tag{1}$$

where $\varepsilon_{ij}^{dil.}$ is represented as:

$$\varepsilon_{ij}^{dil.} = \frac{1}{3}\Sigma\varepsilon_{ii}. \tag{2}$$

By transforming the deviatoric strain tensor from the Cartesian coordinates attached to the unit cell with orientation matrix L, via $\varepsilon'_{lm} = L'_{ij}L^T$, to the sample frame (x, y, z), we can then determine the orientation of the principal axes of the strain ellipsoid in the sample reference frame by standard eigen decomposition. The elastic strain distortion can then be geometrically visualized as an ellipsoid that has transformed from a unit sphere (Fig. 6b, e.g. Nye 1957). This analysis is performed generally as follows:

Given any symmetric second-rank tensor,

$$A_{ij} = \begin{pmatrix} \varepsilon_{xx} & \varepsilon_{xy} & \varepsilon_{xz} \\ \varepsilon_{yx} & \varepsilon_{yy} & \varepsilon_{yz} \\ \varepsilon_{zx} & \varepsilon_{zy} & \varepsilon_{zz} \end{pmatrix} \quad i, j = x, y, z. \tag{3}$$

The eigenvalues are determined by solving the linear transformation equation (4), where for nontrivial solutions the determinant of coefficients on n_j must vanish, leading to (5) which yields a characteristic polynomial of $n = 3$. Each solution λ corresponds to a principal strain value for the system, here in the convention of most negative as compressive, most positive as extensive, with the intermediate value between these two.

$$A_{ij}\ n_j = \lambda\delta_{ij}n_j \rightarrow \left(A_{ij} - \lambda\delta_{ij}\right)\ n_j = 0 \tag{4}$$

$$\left|A_{ij} - \lambda\delta_{ij}\right| = 0 \tag{5}$$

$$\left(A_{ij} - \lambda_i\delta_{ij}\right)\ n_j = 0. \tag{6}$$

The associated directions, or eigenvectors n_j, for each principal strain λ are determined by (6).

Combined, these two entities (eigenvalues and associated eigenvectors) provide the geometry of the deviatoric strain ellipsoid (Fig. 6b), whose axes are the eigenvectors scaled by the eigenvalues. As mentioned above, this analysis is equivalent to a linear transformation applied to a unit sphere, or idealized spherical 'grain', becoming distorted into an ellipsoid where the acting linear operator is the deviatoric strain tensor. Given that this procedure can be performed over a sample area, one can then reconstruct the overall state of strain for the given sample.

The position of the Laue spots (reflections) provide the shape of the deformed unit cell using a non-linear optimization algorithm that minimizes the distances between the measured angular positions of the Laue spots and those calculated from a deformed unit cell at constant volume (Tamura 2014). This provides the unit cell deformation T:

$$T = R^{-1}R_0, \tag{7}$$

where R_0 and R are the transformation matrices converting Cartesian coordinates into unit cell coordinates for the undeformed and deformed unit cell, respectively.

The deviatoric strain tensor can then be obtained through the relation:

$$\varepsilon_{ij}^{dev}\ \frac{T_{ij} + T_{ji}}{2} - \delta_{ij}, \tag{8}$$

where δ_{ij} is the Krönecker symbol.

If we are only interested in the magnitudes of strain, from the tensor we can calculate an 'equivalent strain' ε_{eq} (9), which is commonly expressed in units of microstrain x (10^3) (Liu 2005). This approach was applied in previous work on residual strain in quartz (e.g. Kunz *et al.* 2009, Chen *et al.* 2015)

$$\varepsilon_{eq} = \Big(\left(\varepsilon_{xx} - \varepsilon_{yy}\right)^2 + \left(\varepsilon_{xx} - \varepsilon_{zz}\right)^2 + \left(\varepsilon_{yy} - \varepsilon_{zz}\right)^2 + 6\left(\varepsilon_{xy}^2 + \varepsilon_{xz}^2 + \varepsilon_{yz}^2\right)\Big)^{\frac{2}{3}}. \tag{9}$$

Table 1. List of samples. Quartz vein from Bastogne boudinage (Chen *et al.* 2016a) and seven quartzite samples from the Bergell with locations and Swiss coordinates (km), scan size and step size as well as maximum (0001) pole densities (mrd) from neutron diffraction measurements (Wenk *et al.* 2019).

Sample #	Location	Coordinates	Scan size, steps μm	Neutron mrd
Be-D1	Bastogne		1000 × 3000, 10	
Brg 1126	Avers	757.3/149.4	1500 × 1000, 10	3.6
Brg 1127	Campsut	756.1/151.5	500 × 500,3	3.4
Brg 1135	Septimer	767.6/142.7	1500 × 1000, 10	2.3
Brg 1137	Val Turba	768.1/142.6	1500 × 1000, 10	3.9
Brg 1477	Bugna	760.9/135.45	1500 × 1000, 10	2.9
Sci 690	Innerferrera	756.0/152.1	2000 × 1500, 10	5.8
Sci 881	Passo Turbine	757.0/136.0	2000 × 1500, 10	3.9

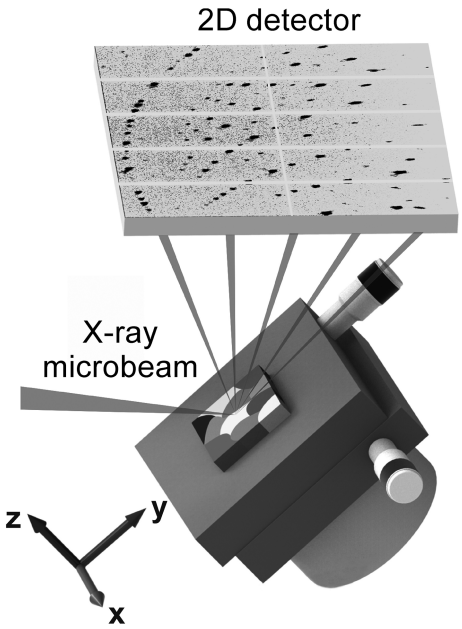

Figure 4. Schematic sketch of Laue diffraction measurements with synchrotron X-ray microdiffraction at ALS; *xyz* is the sample coordinate system. The sample is mounted on a translational stage tilted 45°.

From here, with knowledge of the elastic properties for the material in question, the residual stress associated with the deviatoric portion of the residual strain can then be computed with generalized Hooke's law $\sigma_{ij} = C_{ijkl}\ \varepsilon_{kl}$, where C_{ijkl} is the 4th rank stiffness constant tensor. Note that we use the stiffness tensor of ideal quartz (e.g. Levien *et al.* 1980; Ogi *et al.* 2006), which is only an approximation, since the true tensor in the polycrystal with defects varies.

In previous studies we have discovered that the ε_{yz} component of the strain tensor is quite sensitive to the reflection geometry described above and the sample alignment. Misalignments generally manifest as anomalously high values for this component. Here, we concentrate on the directions of strain rather than the overall magnitudes and explore the possibility to use lattice distortion as a direction-sensitive palaeo-piezometer.

2.3 Laue image analysis with XMAS

The large number of Laue diffraction images are analysed using the software package XMAS (Tamura 2014; Kou *et al.* 2018) to determine the crystal orientation and elastic strain tensor at each position. Input is the 2-D diffraction image (Fig. 5), the calibration of the instrument (obtained with the Si standard or a single crystal quartz standard), the unstrained lattice parameters of quartz, as well as diffraction intensities based on the crystal structure (the crystal data of Gualtieri 2000, are used), and elastic properties of quartz to convert strain to stress (Ogi *et al.* 2006). The XMAS analysis follows a multiple step procedure:

First, the Laue image is corrected to remove bad pixels and a background (typically low for quartz as there is no significant fluorescence signal) is fitted and subtracted.

Secondly, the reflections are automatically found and fitted to 2-D Gaussian functions and classified in decreasing integrated intensity order.

Thirdly, each Laue pattern is indexed to determine the orientation of the crystal lattice relative to sample coordinates, which is defined in XMAS by a matrix. The diffraction intensities have to be taken into account to obtain the correct orientation of trigonal quartz crystal with a hexagonal lattice (Chen *et al.* 2012).

In a fourth step, the difference between the observed positions of diffraction peaks and the ones computed based on the unstrained lattice are used to calculate the deviatoric strain tensor ε' ($\varepsilon' = \varepsilon_{tot} - \varepsilon$; ε_{tot} = total strain, ε = hydrostatic strain component, eq. 1) relative to sample coordinates x, y, z. Deviatoric strain is expressed by a 3 × 3 symmetric matrix with 6 components XX, YY, ZZ, XY, XZ and YZ, relative to sample coordinates x, y, z, similar to the crystal orientation matrix, as described in Section 2.2.

The steps are applied iteratively to all the Laue images. As indexing is by far the most time consuming process, parallel computing on a cluster is performed to analyse the scans at a faster rate (Zhou *et al.* 2018).

3 TEST WITH BOUDINAGE SAMPLE Be-D1

XMAS produces a binary file (.seq) with results from the Laue indexing for each spot on the sample. This includes position of the image in sample coordinates x, y, matrices defining the crystal axes and strain axes relative to sample coordinates, and parameters describing the quality of the fit, for example the number of indexed reflections on an image. For better visualization of the data, this information is then processed with a MATLAB code XtalCAMP (Li *et al.* 2015)). Before proceeding to metamorphic quartzites we will first test experimental procedures and data analysis by returning to a quartzite sample from Bastogne with a vertical string of boudins (Be-D1, Fig. 7a, Chen *et al.* 2016a).

Matrix notation for crystal orientation is converted to Euler angles that are conventionally used in texture analysis. The three Euler

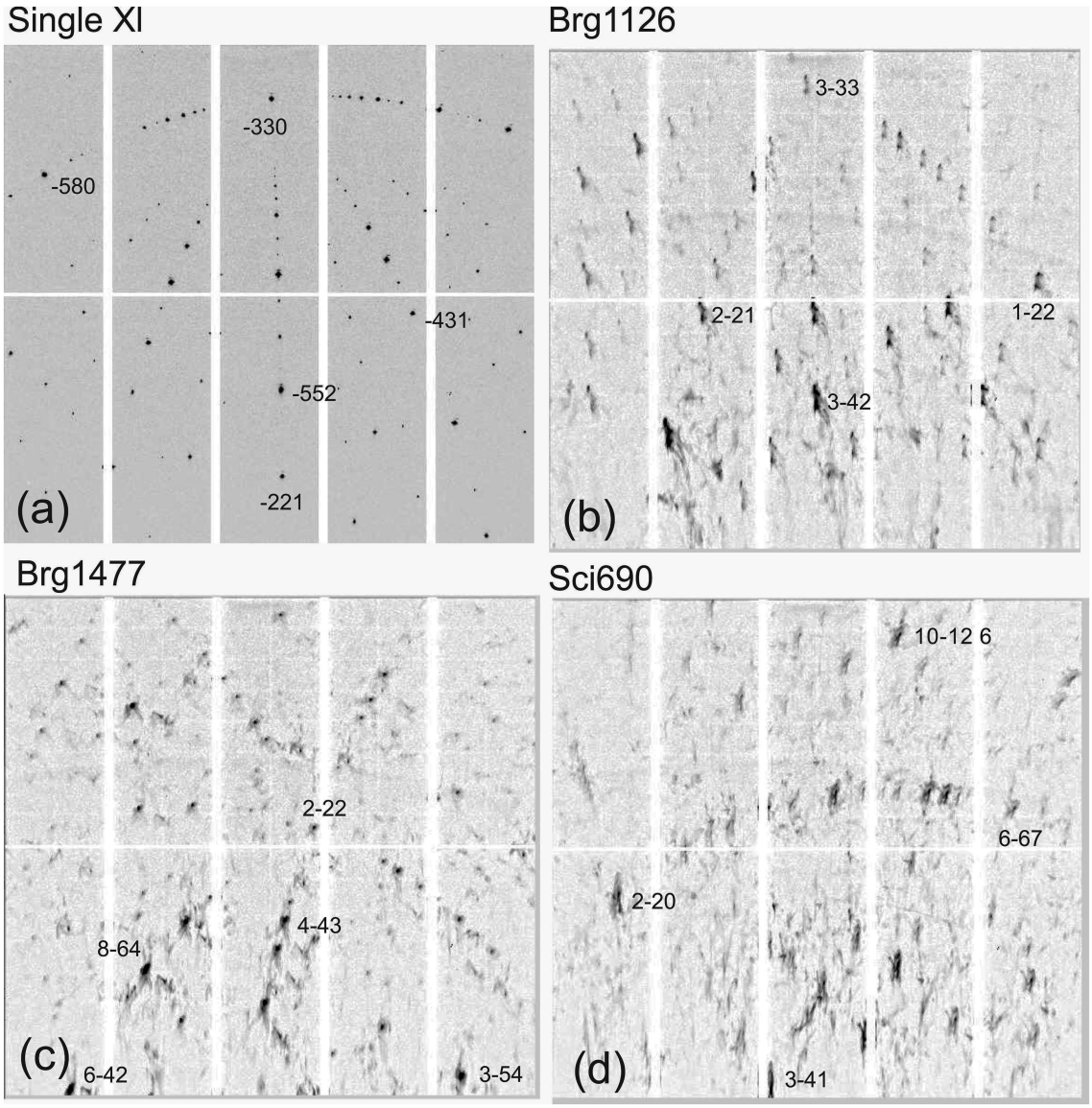

Figure 5. (a–d). Four typical Laue diffraction patterns observed in scans. Streaking is indicative of lattice distortion. (a) Single crystal standard, (b) Brg1126 with splits of an individual crystal into two domains, (c) Brg1477 with minor streaking and (d) Sci690 strong streaking.

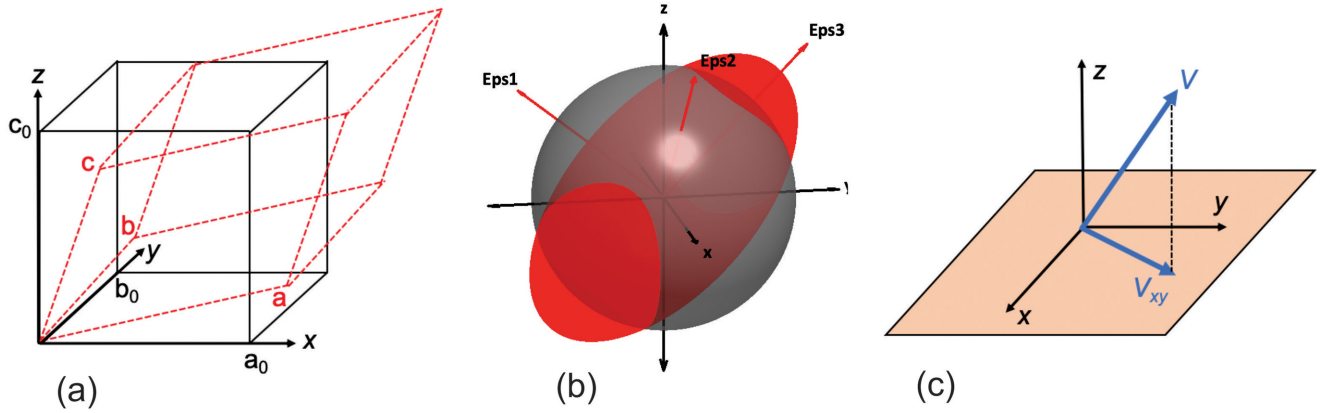

Figure 6. (a) Unit cell of a cubic crystal (black, lattice parameters a_0, b_0, c_0) distorted by strain into a triclinic shape (red, a, b, c). (b) A sphere is distorted into a strain ellipsoid (red) relative to sample coordinates x, y, z. Eps1, Eps2 and Eps3 are ellipsoid axes. (c) Ellipsoid axis described by a vector V relative to sample coordinates x, y, z. The vector is then projected on the sample plane (V_{xy}). This method will be used to map directional strain.

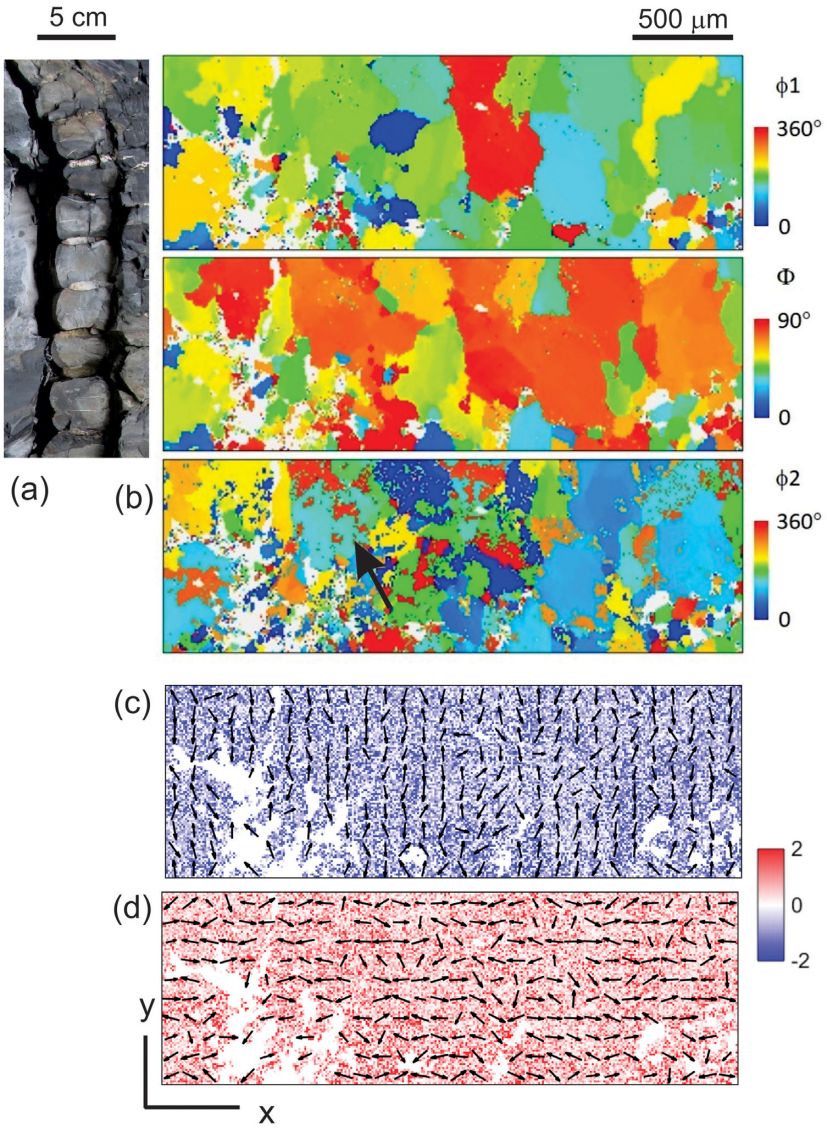

Figure 7. Sample Be-D1 from a quartz layer in Bastogne boudinage (Chen *et al.* 2016a). (a) Boudinage string in the field. (b) Laue microfocus scans displaying the microstructure with Bunge Euler angles (ϕ_1 Φ ϕ_2). Dauphiné twins are visible in the ϕ_2 map (e.g. arrow). (c) Map of compressive strain. Arrows are projections of the principal compressive strain axis projected on the sample plane. The tip of the arrow indicates how the vector points up. (d) Same for extensional strain. Units are 1000× microstrains. White areas could not be indexed.

angles are three rotations that define the orientation relationship between the crystal coordinate system and the sample coordinate system *xyz*. Of the three angles in Bunge convention φ_1, Φ, φ_2 (Bunge 1969, see also Matthies *et al.* 1988 for trigonal crystal symmetry), φ_1 is the azimuth and the angle Φ the pole distance to define the orientation of the crystal *c*-axis relative to sample coordinates, and φ_2 is the rotation around **c** that defines the orientation of the crystal **a**-axis.

Maps of the three Bunge angles are shown for a quartz layer between boudin fragments (Fig. 7b). On these maps we can recognize different grains. White areas indicate positions where Laue images could not be satisfactorily indexed, that is images where fewer than 20 spots could be indexed. In φ_2 maps, some grains are divided into two colours (e.g. black arrow). The colour difference can be identified as a 60° rotation around **c** and corresponds to Dauphiné twins (both host and twin share the **c**-axis). These twins are common in quartz, both as growth twins and as deformation twins (e.g. Minor *et al.* 2018).

Below the Euler angle plots that display the microstructure there are two maps that display with colour the magnitudes of the principal residual strain ellipsoid axes, compression (blue, Fig. 7c) and extension (red, Fig. 7d), ranging from −2000 microstrains to +2000 microstrains. As the colour pattern indicates the residual strain magnitudes are not uniform. Superposed on the colour pattern are arrows that represent the orientation of the strain axes projected on the *xy* map (Fig. 6c). The arrow length indicates how much the axis is tilted out of the *xy* plane and the tip of the arrow indicates that it is tilted up (in the +*z* direction). You can visualize such maps in a similar way as the orientation of schistosity planes or lineation directions are represented on macroscopic geological maps to provide a 3-D assessment of geological structures. Contrary to principle strain axes in Figs 7(c) and (d) with arrows pointing out of the *xy* plane, lineations in rocks (e.g. Fig. 1) on geological maps are pointing down.

Compressive strain axes are dominantly aligned along *y* (Fig. 7c), which is parallel to the boudin axis (Fig. 7a). Extensional strain axes are dominantly aligned along *x* but there are local deviations. This

conforms with earlier observations on Bastogne boudinage (Chen *et al.* 2016a).

4 APPLICATION TO QUARTZITE Brg1127

We next apply the method to a tectonically deformed quartzite Brg1127 (Fig. 8). The thin section was scanned over an area 1.5 mm $\times$ 1.5 mm, in 3 μm steps which is a high resolution. For tectonic quartzites with relatively large plastic strain, Laue images are much more complex (Fig. 5) compared with relatively undeformed grains in the boudinage quartz veins. A significant number of images were rejected because of poor indexing of images (white spots in Fig. 8a). Also, secondary phases such as muscovite, could not be indexed as quartz (white regions in the upper part). The Φ map displays that most quartz grains are flattened (Fig. 8a). The schistosity plane is horizontal. The ϕ_2 map again illustrates some Dauphiné twins, for example the blue-red grain on the left-hand side.

On the right-hand side of the Euler maps there are (0001) pole figures illustrating crystal preferred orientation with a concentration of (0001) poles perpendicular to the foliation, spreading into a *yz* girdle. There Laue pole figures illustrate relatively poor grain statistics relative EBSD pole figures that were measured on the same sample, in similar areas but averaging over a much larger region. On the Laue Φ map a large blue grain dominates with Φ close to 0°. Φ is the angle between the crystal *c*-axis (0001) and the sample *z*-axis with a high pole density close to the centre of the pole figure.

The first map in Fig. 8(b) displays the number of diffraction peaks that were indexed (n-index) in a single image. It displays significant variations, In the centre there are regions where over 50 diffraction peaks could be indexed (red).

Maps of the six strain components XX, YY, ZZ, XY, XZ, YZ are more complex (Fig. 8b). More data have been excluded for strain calculation than for crystal orientation (e.g. only using a YZ range of from -1×10^{-3} to 1×10^{-3} was used). There is a considerable range of strain components from negative (blue) to positive (red). Overall XX and ZZ are dominantly red indicating extension in the *x* and *z* directions but there are some exceptions such as the blue region representing the blue grain in the Φ map. In this case compression (blue) is close to the sample *z* axis and also the crystal *c*-axis. YY is dominantly blue indicating compression along *y*, the normal to the foliation. The mixed components XY, XZ and YZ indicate deviations from alignments with the main axes. These components are difficult to evaluate intuitively.

The strain pattern becomes more clear in plots of the principal axes (Fig. 8c). They show a dominant alignment of blue arrows along *y* (compression) and red arrows along *x* (extension) but for extension there is considerable variation. The magnitudes are illustrated in histograms which show a peak for compression at -1.1×10^3 microstrains and for extension at $+1.0\times10^3$ microstrains.

Fig. 8(d) is similar to Fig. 8(c) but plotting deviatoric stress axes, applying Hooke's law. It shows maxima -100 and $+90$ MPa.

From the orientation matrix that defines the strain ellipsoid orientation relative to sample coordinates, we can calculate strain Euler angles, treating the ellipsoid like an orthorhombic crystal, and from these Euler angles we can plot ellipsoid axes projected on a 3-D sphere relative to sample coordinates *xyz* with different colours, blue for compression, red for extension and green for intermediate (Fig. 9). Clearly there is compression along *y* which is consistent with the 2-D representation on *xy* maps (Fig. 8c).

A more conventional way to plot 3-D orientation distributions of axes is with pole figures, the same way as pole figures are used for crystal axes [e.g. (0001) of quartz in Fig. 8a]. Pole figures for principal axes of deviatoric strain and stress ellipsoids are plotted in Fig. 10, for example using the software BEARTEX (Wenk *et al.* 1998) based on strain/stress Euler angle distributions. For strain pole figures there is a slightly asymmetric maximum of compression axes close to *y* and a tilted concentration of extension close to *x* (Fig. 10a). The intermediate axis displays a girdle. The asymmetry of the residual strain pole figures may be caused by shear strain. Fig. 10(b) shows stress pole figures. They are very similar to strain pole figures. Actual misorientations of stress and strain axes are small, ranging from 1° to 3°.

The two scans Be-D1 and Brg1127 were used to investigate the distortion of the ideal trigonal quartz crystal in more detail (Table 2). We took Gualtieri (2000) as a reference but there are many other reports which are similar (e.g. Le Page & Donnay 1976, Levien *et al.* 1980, Kihara 1990, Antao *et al.* 2008). Because of the range in wavelengths, Laue diffraction does not provide information about absolute lattice parameters. In this case we normalize to deviations from the lattice parameters of Gualtieri. Average standard deviations are small (in the range of 0.0005 Å and 0.08°). but there is a considerable range of distortions (a: 4.88–4.96 Å, b: 5.37–5.45 Å, α: 89–91°, γ: 119.5–120.4°). These deviations expressing elastic lattice distortion are far above standard deviations, giving us confidence in the derived data.

5 RESULTS FOR QUARTZITES

After introducing the methology and demonstrating the applicability with the boudinage test sample Be-D1 and the quartzite sample Brg1127, we applied the same method to another six samples of greenschist facies quartzites from the Central Alps. Most of these samples have been measured in two orientations by rotating the thin section and results are consistent. Here we will only show data for one orientation, with the schistosity plane vertical (*yz*). Optical microstructures have been shown in Fig. 2. Many samples display deformation lamellae, indicative of deformation and presumably partial causes of residual stress. Also, all samples show undulatory extinction indicative of dislocation structures with subgrain boundaries, consistent with TEM observations (Fig. 3).

Fig. 11 shows Laue maps of Bunge angle Φ and crystal orientation data displayed as quartz (0001) pole figures. There is a larger number of white regions than in the Be-D1 test sample. Part of the white domains are muscovite grains and other regions are heavily deformed quartz grains that could not be indexed satisfactorily. Pole figures from X-ray Laue diffraction compare well with EBSD pole figures collected on the same thin section in similar areas.

Fig. 12 displays strain maps of scans. Grey regions could not be indexed as quartz and these were excluded. We are not showing maps for all strain components as we did for Brg1127 (Fig. 8), but instead plot maps for the principal compressive (blue, left-hand side) and extensional strain ellipsoid axes (red, right-hand side) and corresponding histograms as we did for sample Brg1127 (Fig. 8). On these maps projections of selected vectors (every 8 steps) are shown as black arrows pointing up. If vectors are large, they are close to the *xy* plane.

The maps and histograms show considerable variations in magnitudes of the residual strain and the vectors also illustrate a range in strain directions, though a majority of compressive strain vectors is aligned along *x* (perpendicular to the schistosity plane *yz*). The

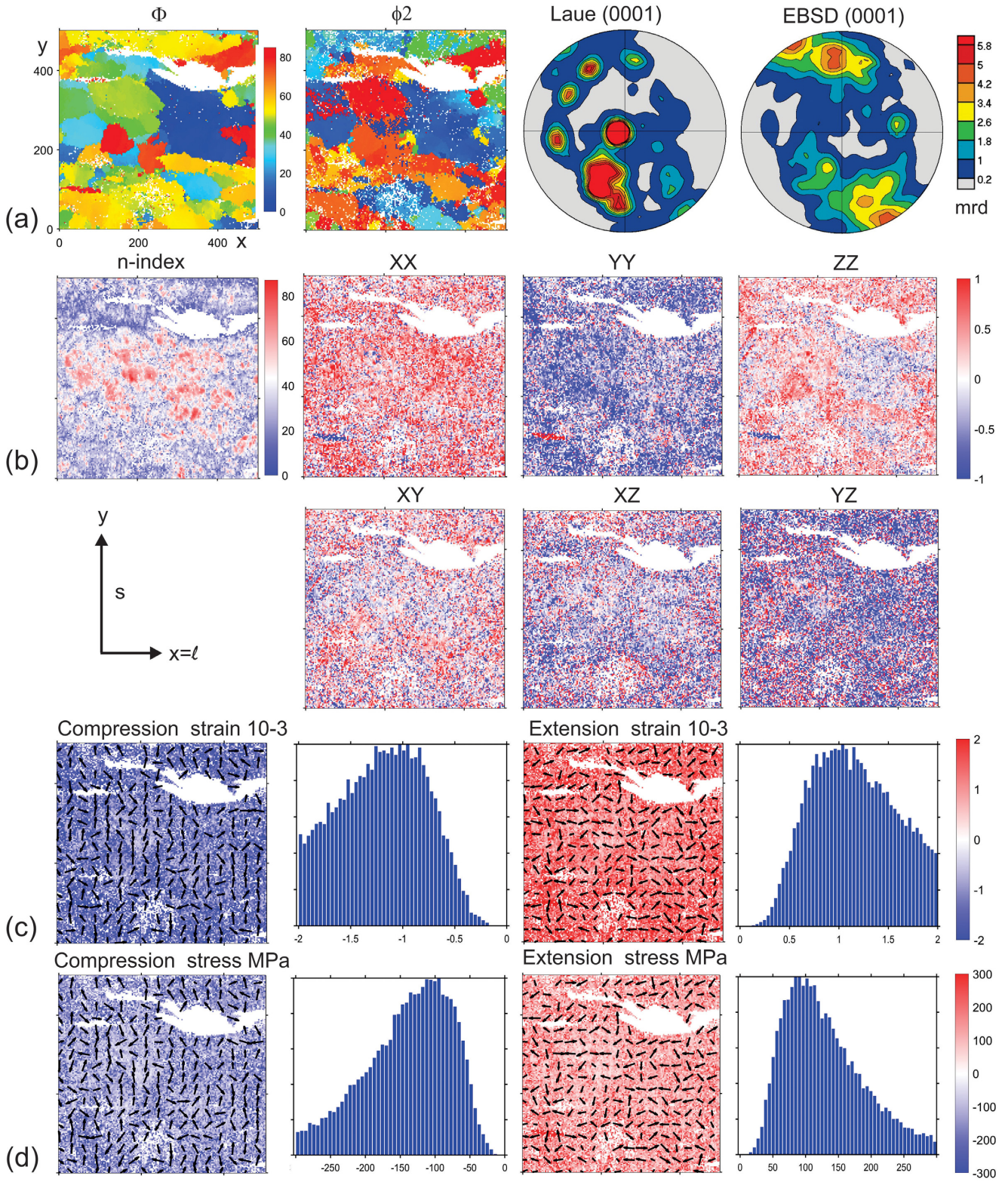

Figure 8. Analysis of sample Brg1127. (a) Microstructure viewed as maps of Euler angles Φ, ϕ_2. To the right-hand side are quartz (0001) pole figures measured by Laue diffraction and EBSD. Equal area projection, pole densities in mrd. (b) Map of n-index, the number of indexed reflections on a Laue image. A large number (red) displays high confidence. Maps of the components of the residual strain tensor XX, YY, ZZ, XY, YZ, relative to sample coordinates. Dominantly blue colours for YY suggest compression in the *y* direction. (c) Maps of the magnitude of the principal residual strain axes (colour scale) and projected arrows give the local strain axis direction (1 of 10 points is shown). Next to the map is a histogram of strain magnitudes (units are 1000 microstrains). (d) Same as (c) but for residual stress calculated from residual strain. Units are MPa.

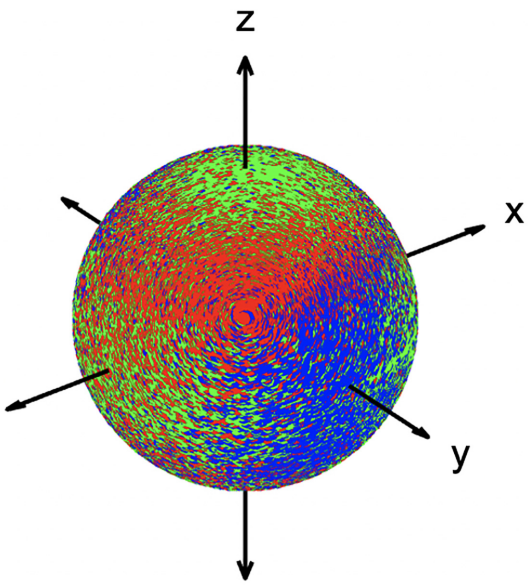

Figure 9. 3-D image of the directions of principal residual strain axes for Brg1127 relative to sample coordinates *xyz*, projected on a sphere. Blue is extension, red is compression, and green is intermediate strain axis.

histograms show fairly sharp distributions for Brg1137 and Sci690 and broad distributions (e.g. for Brg1126 and Brg1135). The orientation of strain axes is further quantified in residual strain pole figures which are 3-D representations of principal strain directions on a sphere (Fig. 13). They illustrate quite a range of distributions which will be further discussed below.

6 DISCUSSION

6.1 Crystal preferred orientation

First a few comments about crystallographic preferred orientation. The samples selected for this study are part of a larger investigation of textures in quartzites from the Bergell (Wenk *et al.* 2019). This region has undergone Tertiary metamorphism, ranging from granulite-amphibolite facies near the contact with the Miocene Bergell granite to low greenschist facies in the North. The samples investigated here are all from greenschist facies quartzites that were originally Triassic sandstones. All texture patterns can be characterized as (0001) maxima perpendicular to the schistosity (Fig. 11), often asymmetric and extending into a girdle perpendicular to the lineation. Grains are significantly deformed and there is secondary recrystallization (Fig. 2). Based on polycrystal plasticity modelling, crystallographic preferred orientation can best be explained by slip on rhombohedral and basal planes, in plane strain deformation (Wenk *et al.* 2019). Asymmetry in the patterns is likely due to a component of simple shear.

It has been impressive to see how well texture patterns measured by Laue diffraction and EBSD compare. Both methods, measured on the same thin sections but not identical regions, provide basically the same results. Here we just show (0001) pole figures but the same is true for *a*-axes and rhombohedral planes. Compared with the two methods illustrated in Fig. 11, neutron diffraction provides better grain statistics by averaging over large volumes but without significant differences. Obviously, of the three diffraction methods EBSD is most easily accessible for texture analysis, both in terms of experiments and data analysis.

6.2 Deviatoric residual strain

Emphasis here is on residual elastic strain and particularly determining the orientation of the deviatoric strain ellipsoid relative to sample coordinates. Magnitudes of deviatoric strain vary from 1000 to 2000 microstrains as illustrated in histograms (Fig. 12). From strain, which is measured as lattice distortion, we can calculate residual stress with magnitudes ranging from −300 to 300 MPa. As the maps show, there is considerable variation in strength which is not clearly related to individual grains as illustrated by comparing Bunge Euler angle maps with strain axes maps (Figs 7, 8, 11 and 12). The variation is also expressed in the spread of orientations as shown with vector directions histograms (Figs 8 and 12) and strain pole figures (Figs 10 and 13). Overall there is a pattern of compressive strain perpendicular to the well-defined schistosity plane which is not surprising since the schistosity can be attributed to shortening during plastic deformation. In many patterns there is asymmetry, presumably due to a contribution of simple shear. The heterogeneity is also observed in microstructures (Fig. 2) and crystal orientations (Fig. 11) but the strain orientation is not directly linked to crystal orientation. The magnitude of the residual elastic strains recorded here are just small fractions of the inelastic finite strains imposed during the geological deformation event but there appears to be a relationship to the larger plastic strains expressed for instance in grain shapes.

6.3 Relationship between crystal directions and strain directions

Is there a relationship between crystal orientation and deviatoric strain tensor orientation? Such a relationship could originate if the assumed *c*/*a* ratio of the unit cell is not correct. There is a range of reported lattice parameters of quartz at ambient conditions (e.g. Levien *et al.* 1980, Kihara 1990; Gualtieri *et al.* 2000; Antao *et al.* 2008) but *c*/*a* ratios are for all very similar. In Fig. 14, we compare misorientations between crystal c-axes and residual strain compression axes for sample Brg1127 and represent them as histograms. There is no clear relationship. For a purely random relationship there should be a sine curve for misorientation statistics (red curve). For the quartzites there may be some trend because in quartzites *c*-axes are centred perpendicular to the schistosity, due to crystal plasticity (Fig. 11), and tectonic stress is also compressive perpendicular to the foliation (Fig. 13). There may be a significant influence of crystal orientation if residual strains develop during phase transformation, for example from hexagonal β to trigonal α quartz.

6.4 Relaxation of strain/stress

Residual stress preserved after relaxation of tectonic strains can be attributed to microstructural defects such as dislocation structures (Fig. 3), deformation lamellae (Fig. 2) and mechanical twins. Deformation lamellae mainly described in shocked quartz (e.g. Vernooij & Langenhorst 2005) but also observed in metamorphic rocks (Christie & Ardell 1974) are common in most samples and Fig. 2 illustrates a diversity of orientations relative to the schistosity plane. They also occur in very low-grade quartz veins in psammitic slates from Bastogne, where residual strain has been documented (fig. 1c in Chen *et al.* 2016a).

Residual lattice strain in quartz recorded in thin sections is related to macroscopic forces applied during tectonic events in a metamorphic geological environment. These rocks originally formed at elevated temperatures and pressures and bringing them to ambient

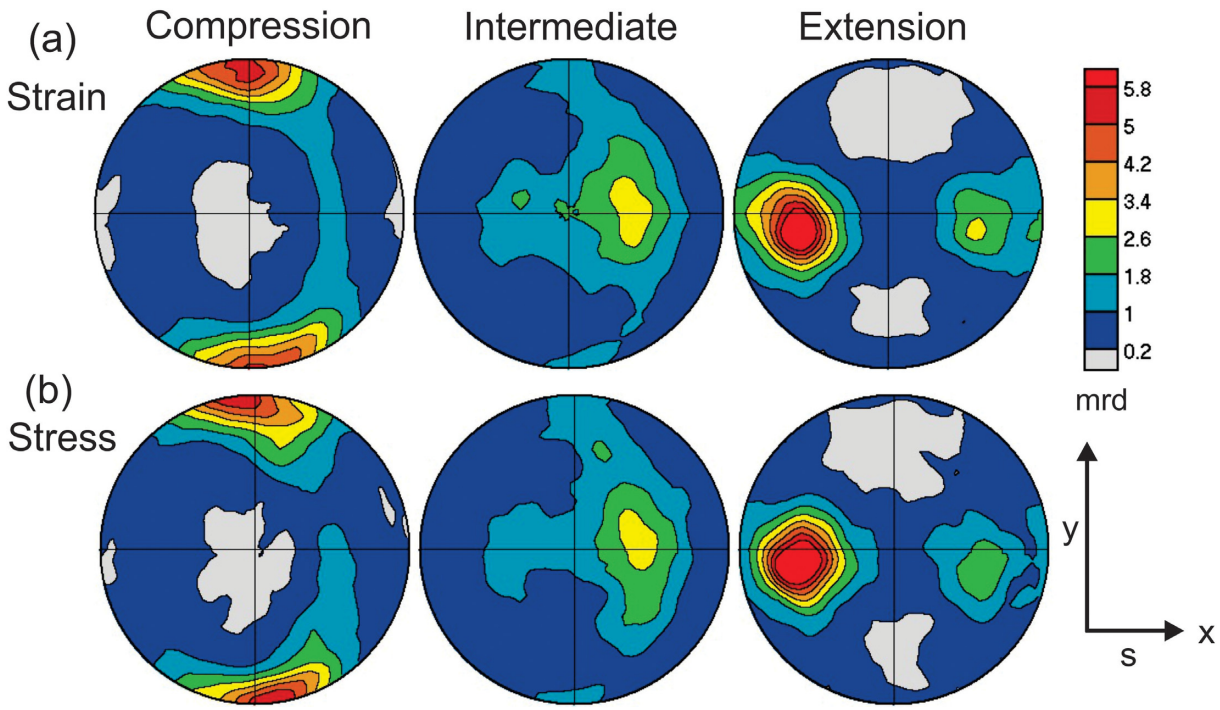

Figure 10. From the 3-D distribution of strain axes 'pole-figures' of the axes of the strain ellipsoid (top) and stress ellipsoid (bottom) can be obtained and are shown for sample Brg 1127. Equal area projection on *xy* plane. Schistosity *s* is *xz*, lineation l is x.

Table 2. Comparison of lattice parameters, ratios, and intra-axis angles between an ideal trigonal quartz (Gualtieri 2000) and the distorted lattices measured in samples Be-D1 and Brg1127 provided the average with accompanying mean standard deviation, maximum and minimum values.

	a	*b*	*c*	*c*/*a*	*c*/*b*	*a*/*b*	α	β	γ
Gualtieri (2000)									
	4.9158	4.9158	5.4091	1.1003	1.1003	1.0000	90	90	120
Be-D1									
Average	4.9110	4.9110	5.4030	1.1002	1.1001	1.0000	90.001	90.007	120.003
St. dev	0.0003	0.0004	0.0005	0.0011	0.0011	0.0007	0.076	0.078	0.054
Min	4.8820	4.8900	5.3681	1.0895	1.0878	0.9927	89.013	89.328	119.460
Max	4.9675	4.9463	5.4404	1.1119	1.1119	1.0091	90.744	91.081	120.413
Brg1127									
Average	4.9221	4.9210	5.4152	1.1001	1.1004	1.0002	90.007	90.001	120.001
St. dev	0.0004	0.0004	0.0005	0.0020	0.0021	0.0014	0.043	0.062	0.045
Min	4.8830	4.8851	5.3735	1.0835	1.0823	0.9901	89.893	89.955	119.530
Max	4.9591	4.9651	5.4572	1.1168	1.1161	1.0102	90.038	90.074	120.389

conditions may also cause distortions of the crystal lattice. So far we have not observed artefacts that could be due to a relationship of residual strain geometry to the orientation of the thin section, or to thin section preparation, but this should be explored in detail in the future. Relationships between crystal orientation and residual strain are likely important to consider for elastically very anisotropic minerals such as mica.

6.6 Limitations of the method

As was mentioned earlier the Laue microdiffraction method was used to determine equivalent strain as an estimate of strain magnitudes. There are severe limitations when this is applied to geological samples. The component YZ is very dependent on exact sample alignment in the beam, relative to detector. Also, the indexation of diffraction images can be difficult for highly deformed grains, which can add a lot to equivalent strain (Fig. 5). Including results for such images adds to the overall equivalent strain, while excluding them produces much lower values and may cause arbitrary selections. The magnitude of residual strain also depends on a reliable *c*/*a* ratio estimate.

The issues discussed above relate to experiments. We mentioned earlier that only a small fraction of the original elastic strain is preserved that was applied during the geological deformation event. The amount depends on the type of microstructural defects that preserve elastic strains and there is very little information in this regard. Yet the very regular strain direction patterns that are observed support the significance.

The seven selected quartzites are all from low metamorphic grade and quartz was at all stages in the trigonal low temperature phase (α-quartz). It should be mentioned that the pattern is very different for high-grade quartzites where quartz was hexagonal during the deformation. Such residual elastic strains in quartz that has undergone the $\beta-\alpha$ transition will be the subject of a future study.

So far all experiments were conducted at the μXRD beamline 12.3.2. of ALS. A new beamline TPS21a at NSRRC in Taiwan

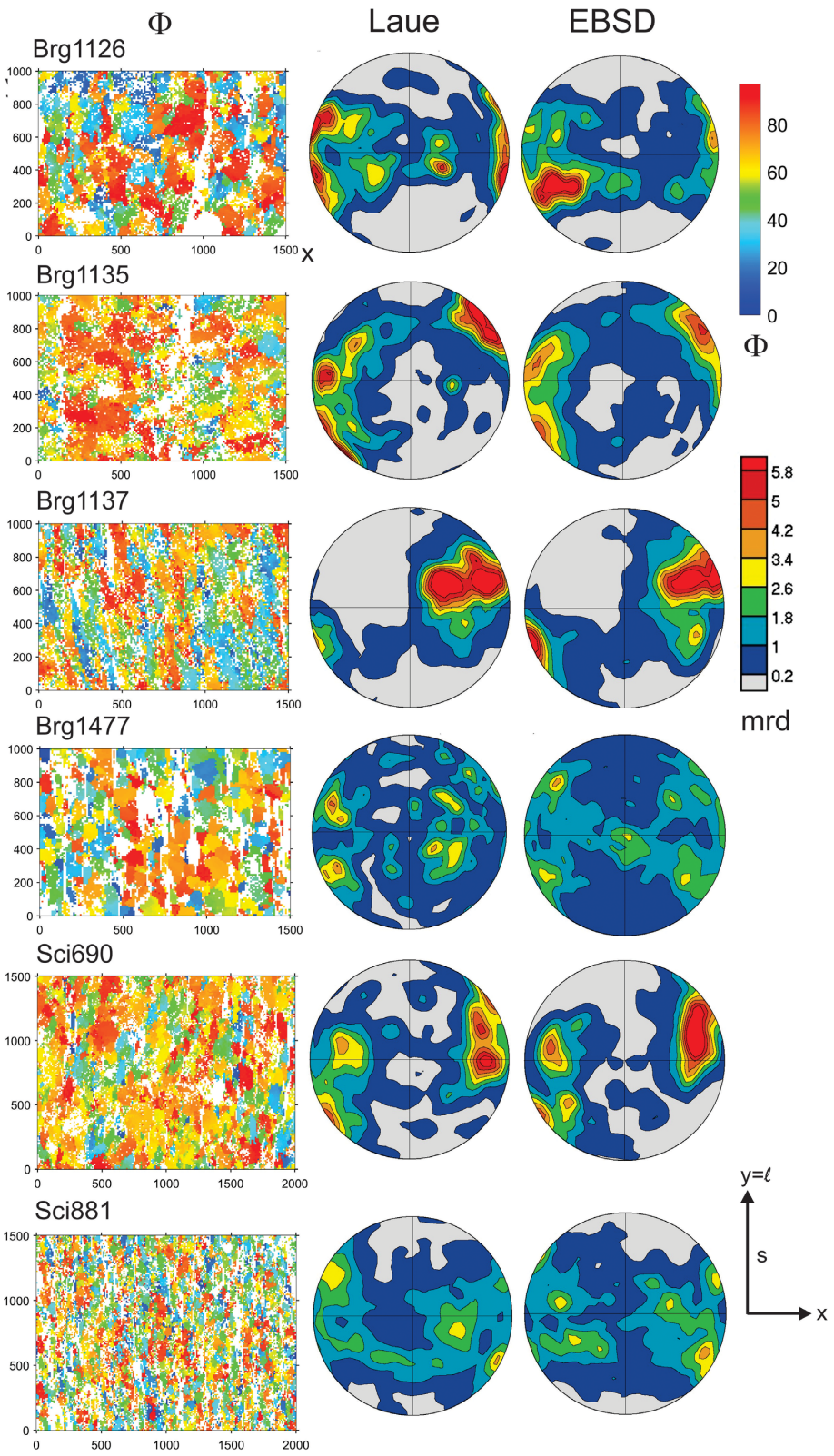

Figure 11. Crystallographic textures of Bergell quartzites. On the left-hand side are maps of Euler angle Bunge2 (Φ) to illustrate grain microstructure, and (0001) pole figures of quartz, comparing Laue diffraction measurements (left-hand side) with and EBSD (right-hand side) on the same thin section on similar areas. Equal area projection. Schistosity plane is vertical (*yz*). White regions could not be indexed as quartz. Most of it is muscovite.

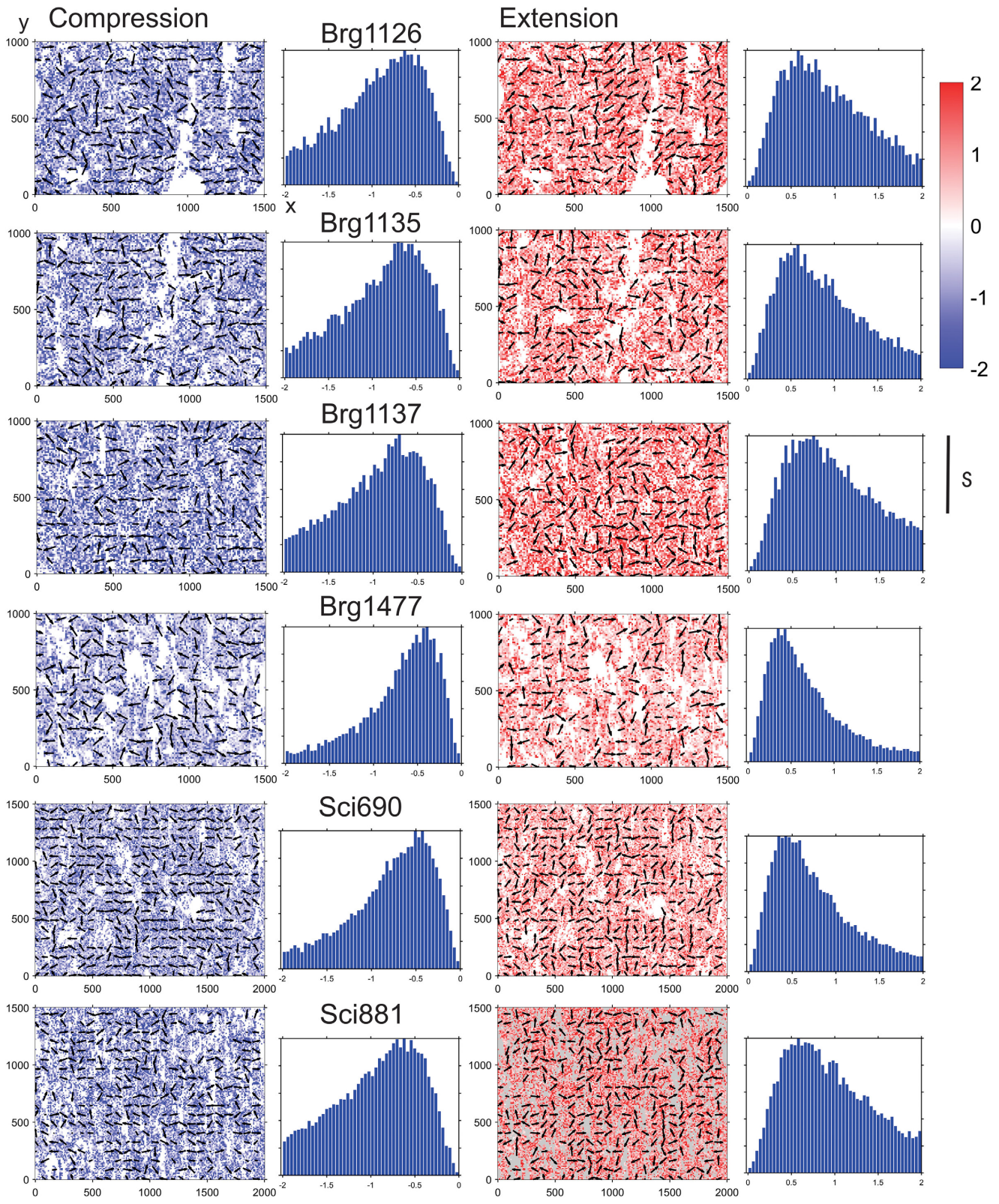

Figure 12. Maps of compressive (blue) and extensional (red) principal residual strain axes. Colour changes indicate deviatoric strain magnitudes (in 10^3 microstrains). For selected positions (1 in 8) vectors of the strain ellipsoid axes are shown, projected on *xy* sample plane. Arrows point up. Schistosity plane is vertical (*yz*). On the right-hand side are histograms for compressive and extensional principal strain.

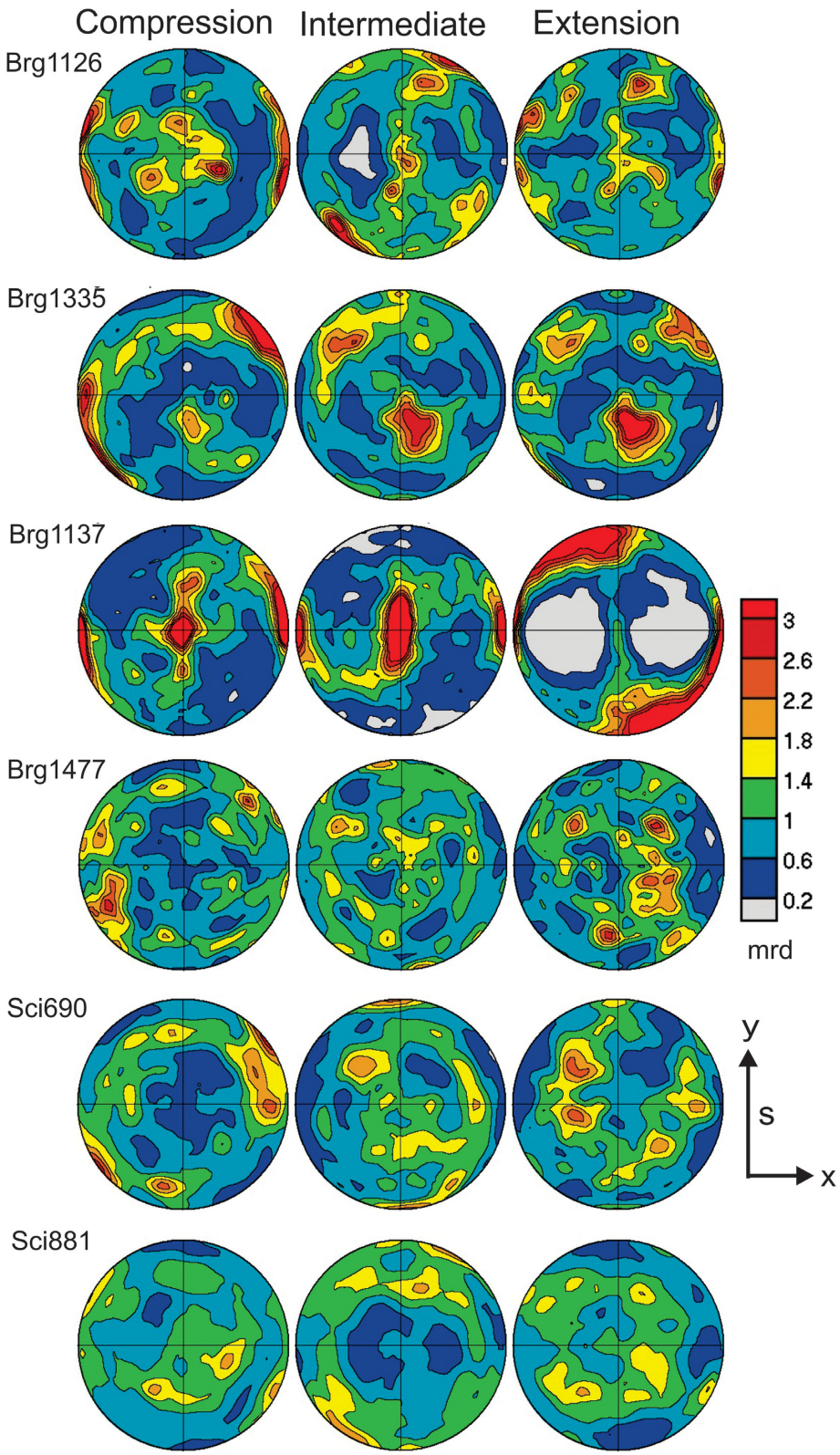

Figure 13. Pole figures of deviatoric residual strain ellipsoid axes (shortening, intermediate and extensional) relative to the sample coordinate system *xyz*, *yz* is schistosity plane. Equal area projection. Contours in multiples of random distribution.

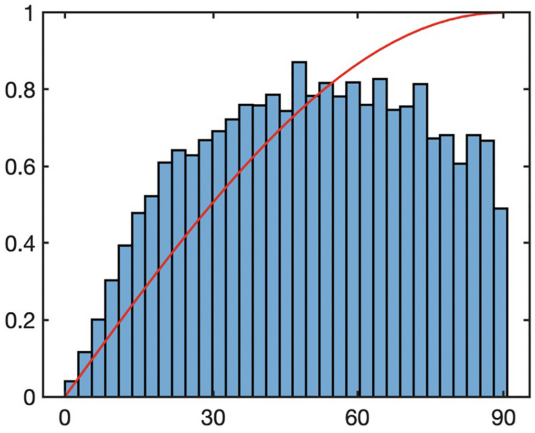

Figure 14. Histogram of angle between crystal *c*-axis and deviatoric strain compression directions for Brg1127. The red curve shows the distribution for a fully random relationship.

greatly exceeds the ALS conditions with a beamsize of ∼0.01 μm and a much higher detector resolution. This opens the possibility for very fine scans to explore, for example, the importance of local defect structures within grains on residual strains (e.g. Chen *et al.* 2016a; Merola *et al.* 2019).

6.7 Potential palaeo-piezometer

Here we have introduced strain and stress pole figures as a new tool to display principal directions of residual strain and stress in deformed rocks. It opens the way to use lattice distortions measured with X-ray diffraction as a palaeo-piezometer, that is to obtain information about the tectonic history and refine the stress field in the Earth's crust (e.g. Zang and Stephansson 2009; Hardebeck 2015). But this is just the beginning and much future work is needed. Experiments need to be refined and the data analysis needs to be improved to establish the method as a reliable tool. In the future the method needs to be applied to rocks from different temperature–pressure environments and different tectonic histories and particularly to experimentally deformed quartz aggregates for which the deformation geometry is known.

7 CONCLUSIONS

During tectonic deformation minerals undergo plastic deformation but in the course crystals are also elastically distorted. This is expressed in the geometry of the crystal lattice which deviates from the ideal undeformed crystal. Some of this elastic distortion is preserved when the macroscopic stress is removed, due to trapping by microstructural defects in the crystal structure. The distortion is particularly easy to record for quartz which has a relatively high crystal symmetry and no significant chemical variations. Directional residual stress has been documented for quartz veins in boudinage and now for metamorphic quartzites. Future applications are necessary to establish the method as a palaeo-piezometer to be used in structural geology.

ACKNOWLEDGEMENTS

We acknowledged access to beamline 12.3.2 of the Advanced Light Source at Lawrence Berkeley National Laboratory as well as use of LBNL computational facilities for data processing. Tim Teague helped with sample preparation as well as EBSD analyses. HRW is appreciative for support from NSF (EAR 1343908) and DOE (DE-FG02-05ER15637) and encouragement from James Rustad. Part of the study was performed while he was on a Fulbright Fellowship at the University of Salamanca, Spain. BCC received an ALS Doctoral Fellowship. RY acknowledges support from Key Science and Technology Program of Shaanxi Province, China (No. 2015GY101). We are grateful to three reviewers, N. Hunter, A. Kronenberg and L.G. Morales, as well as from Michelle Devoe for detailed comments that helped us to improve the manuscript.

REFERENCES

Antao, S.M., Hassan, I., Wang, J., Lee, P.L. & Toby, B.H., 2008. State-of-the-art high resolution powder diffraction (HRPXRD) illustrated with Rietveld structure refinement of quartz, sodalite, tremolite, and meionite, *Can. Mineral.,* **46,** 1501–1509, doi:10.3749/canmin.46.5.1501.

Britton, T.B., Jiang, J., Karamched, P.S. & Wilkinson, A.J., 2013. Probing deformation and revealing microstructural mechanisms with cross-correlation-based, high resolution electron backscatter diffraction, *JOM,* **65**(9), 1245–1253, doi:10.1007/s11837-013-0680-6.

Britton, T.B. & Wilkinson, A.J., 2011. Measurement of residual strain and lattice rotations with high resolution electron backscatter diffraction, *Ultramicroscopy,* **111,** 1395–1404,doi: 10.1016/j.ultramic.2011.05.007.

Bruehl, H., 1969. Boudinage in den Ardennen und in der Nordeifel als Ergebnis der inneren Deformation, *Geologische Mitteilungen,* **8,** 263–308.

Bunge, H.J.,1969. *Mathematische Methoden der Texturanalyse,* Akademie Verlag, 330 pp.

Chen, K., Dejoie, C. & Wenk, H.-R., 2012. Unambiguous indexing of trigonal crystals from white beam Laue diffraction patterns: application to Dauphiné twinning and lattice stress mapping in deformed quartz, *J. Appl. Cryst.,* **45,** 982–989, doi:10.1107/S0021889812031287.

Chen, K., Kunz, M., Li, Y., Sintubin, M., Zepeda, E. & Wenk, H.-R., 2016a. Compressional residual stress in Bastogne boudins revealed by synchrotron X-ray microdiffraction, *Geophys. Res. Lett.,* **43,** 6178–6185, doi:10.1002/2016GL069236.

Chen, K., Kunz, M., Tamura, N. & Wenk, H.-R., 2015. Residual stress preserved in quartz from the San Andreas Fault Observatory at Depth, *Geology,* **43**(3), 219–222, doi:10.1130/G36443.1.

Chen, K., Kunz, M., Tamura, N. & Wenk, H.-R. 2011. Evidence for high stress in quartz from the impact site of Vredefort, South Africa, *Eur. J. Mineral.,* **23,** 169–178, doi:10.1127/0935-1221/2011/0023-2082.

Chen, X., Dejoie, C., Jiang, T., Ku, C.-S. & Tamura, N., 2016b. Quantitative microstructural imaging by scanning Laue x-ray micro- and nanodiffraction. *MRS Bull.*, **41,** 445–453, doi:10.1557/mrs.2016.97.

Christie, J.M. & Ardell, A.J., 1974. Substructures of deformation lamellae in quartz, *Geology,* **2,** 404–408.

Clausen, B., Lorentzen, T., Bourke, M.A.M. & Daymond, M. R., 1999. Lattice strain evolution during tensile loading of stainless steel, *Mater. Sci. Eng. A,* **259,** 17–24, doi:10.1016/S0921- 5093(98)00878-8.

Derez, T., Penncock, G., Drury, M. & Sintubin, M., 2015. Low-temperature intracrystalline deformation microstructures in quartz, *J. Struct. Geol.,* **71,** 3–23, doi 10.1016/j.jsg.2014.07.015.

Fossen, H., 2016. *Structural Geology,* 2nd edn, Cambridge Univ. Press, 480 pp, IBSN 978-1-107-05764-7.

Friedrich, W., Knipping, P. & Laue, M., 1912. Interferenzerscheinungen bei Röntgenstrahlen. *S.B. bayerische Akad. Wiss.,* **14,** 303–322.

Goscombe, B.D., Passchier, C.W. & Hand, M., 2004. Boudinage classification: end-member boudin types and modified boudin structures, *J. Struct. Geol.,* **26**(4), 739–763, doi:10.1016/j.jsg.2003.08.015.

Gualtieri, A.F. 2000. Accuracy of XRPD QPA using the combined Rietveld-RIR method. *J. Appl. Cryst.,* **33,** 267–278, doi:10.1107/S002188989901643X.

Hamers, M.F. & Drury, M.R., 2011. Scanning electron microscope-cathodoluminescence (SEM-CL) imaging of planar deformation features

and tectonic deformation lamellae in quartz, *Meteor. Planet. Sci.,* **46/12,** 1814–1831, doi: 10.1111/j.1945- 5100.2011.01295.x.

Hardebeck, J.L., 2015. Stress orientations in subduction zones and the strength of subduction megathrust faults, *Science,* **349**(6253), 1213–1216, doi: 10.1126/science.aac5625.

Hosford, W. F., 2005. Residual stresses. In *Mechanical Behavior of Materials,* pp. 308–321. Cambridge Univ. Press. ISBN 978-0-521-84670-7.

Hutchings, M.T., Withers, P.J., Holden, T.M. & Lorentzen, T., 2005. *Introduction to the Characterization of Residual Stress by Neutron Diffraction*. CRC Press, ISBN 9780367393267.

Ice, G.E., Budai, J.D. & Pang, J.W., 2011. The race to x-ray microbeam and nanobeam science, *Science,* **334,** 1234–1239, doi: 10.1126/science.1202366.

Kang, K. J., Yao, N., He, M.Y. & Evans, A.G., 2003. A method for in situ measurement of the residual stress in thin films by using the focused ion beam, *Thin Solid Films,* **443,** 71–77, doi:10.1016/S0040-6090(03)00946-5.

Kelleher, J., Prime, M.B., Buttle, D., Mummery, P.M., Webster, P.J., Shackleton, J. & Withers, P.J., 2003. The measurement of residual stress in railway rails by diffraction and other methods, *J. Neutron Res.,* **11,** 187–193, doi:10.1080/10238160410001726602.

Kihara, K., 1990. An X-ray study of the temperature dependence of the quartz structure, *Eur., J. Mineral*., **2**(1), 63–78, doi:10.1127/ejm/2/1/0063.

Kou, J., Chen, K. & Tamura, N., 2018. A peak position comparison method for high speed quantitative Laue microdiffraction data processing, *Scripta Mat*., **143,** 49–53, doi:10.1016/j.scriptamat.2017.09.005.

Kruhl, J.H., Wirth, R. & Morales, L.F.G., 2013. Quartz grain boundaries as fluid pathways in metamorphic rocks. *J. geophys. Res.* **118,** 1957–1967, doi:10.1002/jgrb.50099.

Kröner, E. & Anthony, K.-H., 1975. Dislocations and disclinations in material structures: the basic topological concept, *Ann. Rev. Mater.,* **5,** 43–72, doi:10.1016/j.scriptamat.2017.09.005.

Kunz, M., Chen, K., Tamura, N. & Wenk, H.-R., 2009. Evidence for residual stress in deformed natural quartz, *Am. Mineral.,* **94,** 1059–1062, doi:10.2138/am.2009.3216.

Le Page, Y. & Donnay, G., 1976. Refinement of the crystal structure of low-quartz, *Acta Cryst*., **B32,** 2456–2459.

Levien, L., Prewitt, C.T. & Weidner, D.J., 1980. Structure and elastic properties of quartz at pressure, *Am. Mineral.,* **65,** 920–930.

Liddel, N. A., Phakey, P.P. & Wenk, H.-R., 1976. The microstructure of some naturally deformed quartzites, in *Electron Microscopy in Mineralogy,* pp. 419–427, eds Wenk, H.-R. *et al.*, Springer-Verlag.

Liu, A.F., 2005. *Mechanics and Mechanisms of Fracture: An Introduction,* ASM International, 654 pp, ISBN 978–0871708021.

Li, Y., Qian, D., Xue, J., Wan, J., Zhang, A., Tamura, N., Song, Z. & Chen, K., 2015. A synchrotron study of defect and strain inhomogeneity in laser-assisted three-dimensionally-printed Ni-based superalloy, *Appl. Phys. Lett.,* **107,** 181902, doi:10.1063/1.4934839.

Lohest, M., Stainier, X. & Fourmarier, P., 1908. Compte rendu de la session extraordinaire de la Société géologique de Belgique., tenu a Eupen et a Bastogne les 29, 30 et 31 aout et le 1, 2 et 3 septembre 1908, *Ann. Soc. Geol. Belgique,* **35,** B351–434.

Lunt, J.G. & Korsunsky, A.M., 2015. A review of micro-scale focused ion beam milling and digital image correlation analysis for residual stress evaluation and error estimation. *Surf. Coat. Technol.,* **283,** 373–388, doi:10.1016/j.surfcoat.2015.10049.

Matthies, S., Wenk, H.-R. & Vinel, G. W., 1988. Some basic concepts of texture analysis and comparison of three methods to calculate orientation distributions from pole figures, *J. Appl. Crystall.* **21,** 285–304, doi:10.1107/S0021889888000275.

Merola, C., Cheng, H.-W., Dworschak, D., Ku, C.-S., Chiang, C.-Y., Renner, F.U. & Valtiner, M., 2019. Nanometer resolved real time visualization of acidification and material breakdown in confinement. *Adv. Mat. Interf.,* **6,** 1802069, doi:10.1002/admi.201802029.

Minor, A., Rybacki, E., Sintubin, M., Vogel, S. & Wenk, H.-R., 2018. Tracking mechanical Dauphiné twin evolution with applied stress in axial compression experiments on a low-grade metamorphic rock, *J. Struct. Geol.,* **112,** 81–94, doi:10.1016/j.jsg.2018.04.002.

Noyan, I.C. & Cohen, J.B., 1987. *Residual Stress: Measurement by Diffraction and Interpretation,* Springer, doi:10.1007/978-1-4613-9570-6.

Nye, J.F., 1957. *Physical Properties of Crystals. Their Representation by Tensors and Matrices,* Oxford Clarendon Press, 322pp.

Ogi, H., Ohmori, T., Nakamura, N. & Hirao, M., 2006. Elastic, anelastic, and piezoelectric coefficients of a-quartz determined by resonance ultrasound spectroscopy, *J. Appl. Phys.,* **100,** 053511, doi:10.1063/1.2335684.

Pintschovius, L.& & Jung, V., 1983. Residual stress measurements by means of neutron diffraction, *Mater. Sci. Eng.,* **61,** 43–50.

Schajer, G.S., 2013. *Practical Residual Stress Measurement Methods*. Wiley. ISBN 978-1-18-34237-4.

Staron, P., Kocak, M. & Williams, S., 2002. Residual stresses in friction stir welded Al sheets, *Appl. Phys., A* **74,** S1161–2, doi:10.1007/s003390201830.

Stefanescu, D., Steuwer, A., Owen, R.A., Nadri, B., Edwards, L., Fitzpatrick, M.E. & Withers, P.J., 2004. Elastic strains around cracked cold expanded fastener holes measured using the synchrotron x-ray diffraction technique, *J. Strain Anal.,* **39,** 459–69, doi:10.1243%2F0309324041896470.

Tamura, N., 2014. XMAS: a versatile tool for analyzing synchrotron X-ray microdiffraction data, in *Strain and Dislocation Gradients from Diffraction,* pp. 125–155, eds Ice, G.E. & Barabash, R., London Imperial College Press, doi:10.1142/9781908979636_fmatter.

Ungar, T., Gubicza, J., Ribarik, G. & Borbely, A., 2001. Crystallite size distribution and dislocation structure determined by diffraction profile analysis: principles and practical application to cubic and hexagonal crystals, *J. Appl. Cryst.,* **34,** 298–310, doi:10.1107/S0021889801003715.

Van Puymbroeck, E., Nagy, W., Schotte, K., Ul-Abdin, Z. & DeBacker, H., 2019. Determination of residual stresses in a steel bridge component by finite element modeling of the incremental hole-drilling method, *MDPI, Appl. Sci.,* **9,** 536, doi:10.3390/app9030536.

Vernooij, M.G.C. & Langenhorst, F., 2005. Experimental reproduction of tectonic deformation lamellae in quartz and comparison to shock-induced planar deformation features, *Meteor. Planet. Sci.,* **40**(9/10), 1353–1361, doi: 10.1111/j.1945-5100.2005.tb00406.x.

Wallis, D., Hansen, L.N., Britton, T.B. & Wilkinson, A.J., 2017. Dislocation interactions in olivine revealed by HR-EBSD. *J. geophys. Res.,* **122,** 7659–7678, doi: 10.1002/2017JBO14513.

Wenk, H.-R., 1966. Fehlbau in Quarzkristallen aus Tektoniten, *Contrib. Mineral. Petrol.,* **12,** 63–72.

Wenk, H.-R., Matthies, S., Donovan, J. & Chateigner, D., 1998. BEARTEX, a Windows-based program system for quantitative texture analysis, *J. Appl. Cryst.,* **31,** 262–269, doi:10.1107/S002188989700811X.

Wenk, H.R., Yu, R., Vogel, S. & Vasin, R., 2019. Preferred orientation of quartz in metamorphic rocks from the Bergell Alps, *MDPI, Miner.,* **9**(5), 277, doi:10.3390/min9050277.

Wilkinson, A.J., Meaden, G. & Dingley, D.J., 2006. High-resolution elastic strain measurement from electron backscatter diffraction patterns: new levels of sensitivity. *Ultramicroscopy,* **106**(4-5), 307–313, doi:10.1016/j.ultramic.2005.10.001.

Withers, P.J., 2007. Residual stress and its role in failure. *Rep. Prog. Phys.,* **70,** 2211–2264, doi:10.1111/j.1475-1305.2001.tb01216.x.

Withers, P.J. & Webster, P.J., 2001. Neutron and synchrotron x-ray strain scanning. *Strain,* **37,** 19–31, doi:10.1111/j.1475-1305.2001.tb01216.x.

Zang, A. & Stephansson, O., 2009. *Stress Field of the Earth's Crust*. Springer, 322 pp., doi:10.1007/978-1-4020-8444-7.

Zhou, G., Kou, J., Li, Y., Zhu, W., Chen, K. & Tamura, N., 2018. Quantitative scanning Laue diffraction microscopy: application to the study of 3D printed nickel-based superalloys. *Quant. Beam Sci.,* **2**(2), 13, doi:10.3390/qubs2020013.